PAPER

Check for updates

Denitrification activity test of a V modified Mn-based ceramic filter

Lei Sun, [ID] *[a] Zhenzhen Wang [ID] [b] and Mengxi Zang[b]

In view of the characteristics of high temperature denitrification and low water and sulfur resistance of single manganese-based catalysts, a vanadium–manganese-based ceramic filter (VMA(14)-CCF) was prepared by the impregnation method modified with V. The results showed that the NO conversion of VMA(14)-CCF was more than 80% at 175–400 °C. At 225–300 °C, the conversion of NO can reach 100%. High NO conversion and low pressure drop can be maintained at all face velocities. The resistance of VMA(14)-CCF to water, sulfur and alkali metal poisoning is better than that of a single manganese-based ceramic filter. XRD, SEM, XPS and BET were further used for characterization analysis. The introduction of V protects the MnO_x center, promotes the conversion of Mn^{3+} to Mn^{4+}, and provides abundant surface adsorbed oxygen. The development of VMA(14)-CCF greatly broadens the application range of ceramic filters in denitrification.

1 Introduction

Nitrogen oxides (NO_x), including NO, NO_2, and N_2O, are the main air pollutants, which can cause a series of environmental problems such as acid rain, photochemical smog, and haze, posing a risk to human health.[1–3] The use of various fuels and vehicles are the main sources of NO_x. To improve the environment and achieve sustainable development of society, the development of new and efficient denitrification technologies has become a research focus in the field of environmental protection.[4–6]

Catalytic ceramic filter (CCF) is a filtration material used for high-temperature gas purification.[7] The dust removal and denitration in high-temperature flue gas can be carried out synchronously in the same device.[8] This approach solves the issues of a lengthy purification process and large footprint associated with separate dust removal and denitrification steps in traditional processes, as well as problems such as catalyst poisoning and erosion caused by dust, alkali metals, and other factors. It can effectively prolong the lifespan of catalysts and reduce denitrification costs. CCF is a novel, promising, and efficient denitrification technology. The catalyst commonly used in CCF is V–W/Ti, and its active temperature range being 300–400 °C. It has poor low-temperature activity.[9] However, V_2O_s exhibit excellent Selective Catalytic Reduction (SCR) activity and strong water and sulfur resistance at high temperatures.

The structure and electronic distribution of metal elements can change due to mutual doping, resulting in differences in catalytic performance under different flue gas conditions.[10–13] Liu *et al.*[14] modified the low-temperature SCR activity of V/Ti catalyst by loading Mn, and the results demonstrated that the addition of MnO_x enhanced the redox capability of V. Thanh *et al.*[15] employed a co-precipitation method to prepare Ce/TiO_2, Mn–Ce/Ti, and Mn–V–Ce/Ti catalysts. They observed a significant reduction in NH_3 oxidation and a substantial improvement in the N_2 selectivity of the catalyst upon simultaneous addition of V and Mn to the Ce/TiO_2 catalyst. Characterization results indicated that this enhancement was due to the synergistic effect between VO^{3+}/VO^{2+} groups in the VO_x species and Mn^{3+}/Mn^{2+} groups in the MnO_x species, which suppressed NH_3 oxidation and thereby increased the N_2 selectivity of these catalysts. Niu *et al.*[16] employed the sol–gel method to incorporate Ce and V into MnO_x/TiO_2 catalysts to suppress the formation of nitric oxide (NO) at low temperatures and enhance the N_2 selectivity of the catalyst. Various techniques, including selectivity, XRD, XPS, NH_3-TPD, and infrared spectroscopy, were utilized for analysis. The results demonstrated that the addition of Ce improved the conversion efficiency of NO, shifting the high-performance region to lower temperatures. Meanwhile, the addition of V reduced the generation of N_2O while maintaining high NO conversion efficiency and low N_2O formation.

However, further research is needed to investigate the coupling of V–Mn composite catalysts with CCF, as well as the SCR reaction mechanism, water resistance, sulfur resistance, and other aspects of V–Mn-based CCF, in both depth and breadth. This study uses a small amount of V-doped Mn/γ-Al_2O_3 to prepare V–Mn/γ-Al_2O_3. V–Mn/γ-Al_2O_3 is loaded on ceramic filter to prepare a CCF with a wide active temperature range,

[a]Anhui Academy for Ecological and Environmental Science Research, Hefei 230071, China. E-mail: sunlei551@qq.com

[b]School of Resource and Environmental Engineering, Hefei University of Technology, Hefei 230009, China

good water and sulfur resistance, and strong alkali resistance, to expand the industrial application range of the CCF. In addition, characterization and analysis using XRD, SEM, EDS, and BET are conducted to investigate the influence of V on the SCR activity of catalyst, as well as the reaction mechanism and poisoning mechanism of V–Mn-based CCF.

2   Materials and methods

2.1   Preparation of catalyst ceramic filter

The precursor $Mn(CH_3COO)_2 \cdot 4H_2O$ (99.9%, Guang Fu, China) was selected for this study. It was combined with γ-Al_2O_3 (AR, Sinopharm Chemical Reagent, China) in a beaker, followed by the addition of a specific quantity of deionized water. After vigorous stirring for 2 h, the mixture was allowed to age for 12 h at a controlled temperature of 40 °C. Subsequently, the impregnated product was subjected to a drying process and then calcined at 400 °C in a muffle furnace, yielding the pristine Mn/γ-Al_2O_3 catalyst. To prepare the V-modified catalyst, the precursor NH_4VO_3 (AR, Aladdin, China) was introduced using the same methodology, resulting in the formation of V–Mn/γ-Al_2O_3.

For experimental purposes, the ceramic filter (Anhui Yiyi Environmental Protection Equipment Co., Ltd) was cut into cylindrical shapes with a length of 20 mm and a diameter of 16 mm. The ceramic filter (CF) was then subjected to a series of treatments including water rinsing, acid treatment, and alkaline treatment. Afterward, CF was placed in an oven and dried at 100 °C, followed by calcination in a muffle furnace at 400 °C for 3 h. The treated CF was carefully weighed and kept for further use.

To prepare the catalyst, it was dissolved in a water solution and polyethylene glycol (PEG) was added. The mixture was then sonicated for 5 min at 40 °C. The catalyst was coated onto the pre-treated CF, which is referred to as the first loading. The CCF prepared using Mn/γ-Al_2O_3 as the catalyst is denoted as MA(x)-CCF, where x represents the loading amount of Mn/γ-Al_2O_3. Similarly, the CCF prepared using V–Mn/γ-Al_2O_3 as the catalyst is denoted as VMA(y)-CCF, where y represents the loading amount of V–Mn/γ-Al_2O_3.

2.2   Sample characterization

The catalyst and the CCF were determined using a Dandong Haoyuan DX-2700 X-ray diffraction (XRD). Since the CCF is solid, the XRD requires the samples to be in powder form. Therefore, the CCF was ground in a mortar and sieved through a 200-mesh sieve. Cu Kα radiation was used, with experimental conditions set at 40 kV (1 kV per step) for tube voltage, 30 mA for tube current, and a scanning rate of 4° min^{-1}. Intensity data was collected in the range of 2θ from 5° to 75°.

The loaded state of the catalyst on the CCF was observed using a scanning electron microscope (SU8020, Hitachi, Japan) with a voltage range of 0.1–30 kV. During the sample preparation process, the CCF was cut into thin slices of 8 mm × 8 mm and attached to a sample stage with black conductive adhesive. Vacuum gold sputtering was performed due to the good

insulation properties of CCF. Energy-dispersive spectroscopy (EDS) was used in conjunction to obtain the element composition and content of the designated area of the tested samples. Since the content of the catalyst in the CCF was only about 10–20%, and the content was low, XPS was directly used to determine the catalyst sample.

The elemental valence state content on the surface of the catalyst sample was determined using an ESCALAB250Xi (Thermo, America) with Al Kα radiation. The XPS spectra were deconvoluted using XPSPEAK4.1. By normalizing the peak areas, surface concentrations of each atom and the proportion of different valence states of each element were calculated.

The specific surface area and pore volume of the catalyst were determined using a BET (Brunauer–Emmett–Teller) surface area and pore size analyzer (3H-2000PS2) by nitrogen adsorption isotherm measurements at liquid nitrogen temperature (77 K). The pore structure information was obtained using the BJH (Barrett–Joyner–Halenda) method.

2.3   Catalytic performance test

The catalytic denitration performance of the CCF was studied in a homemade fixed-bed reactor, as shown in Fig. 1. The flue gas composition used was 500 ppm NH_3, 500 ppm NO, 3 vol% O_2, 100 or 300 ppm SO_2 (when used), and 10 vol% H_2O (when use), with Ar as the balance gas. The outlet gas was analyzed using a flue gas analyzer, and the pressure drop was measured using a differential pressure gauge. The NO conversion is calculated as:

$$NO_{conversion} (\%) = \frac{NO_{in} - NO_{out}}{NO_{in}} \times 100\% \tag{1}$$

3   Results and discussion

3.1   The optimal preparation of catalyst ceramic filter

V–Mn/γ-Al_2O_3 was loaded onto the CCF using a single-step coating method with PEG as the binder, as shown in Table 1. The actual loading rate of the catalyst is calculated by calculating the quality difference of CF load before and after operation. The loading rate was 8.8% after one coating, 14% after two coatings, and 19% after three coatings.
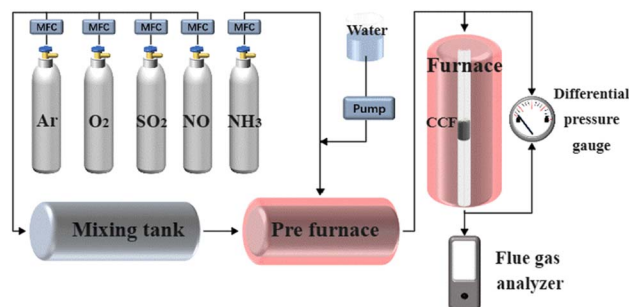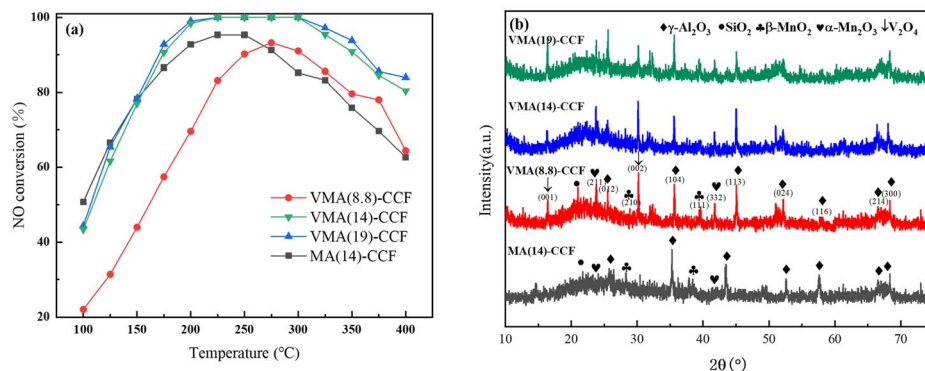

Fig. 1   Experimental device diagram.

Table 1 The influence of the loading number of times on the loading rate of VMA(*y*)-CCF

Sample	VMA(8.8)-CCF	VMA(14)-CCF	VMA(19)-CCF
The loading number of times	1	2	3
The loading rate (%)	8.8	14	19

Fig. 2 (a) NO conversion and (b) XRD patterns of MA(*x*)-CCF and VMA(*y*)-CCF.

The samples with different loading rates were tested for denitration activity, as shown in Fig. 2(a). As the loading amount of V–Mn/γ-Al$_2$O$_3$ increased, the denitration efficiency of VMA(*y*)-CCF gradually increased. However, the increase in NO conversion of VMA(19)-CCF compared to VMA(14)-CCF was not significant, and increasing the number of loadings would increase production costs and filter pressure drop. Therefore, VMA(14)-CCF was chosen as the research object. The NO conversion was greater than 80% at 175–400 °C, and could reach 100% at 225–300 °C. VMA(14)-CCF exhibited excellent
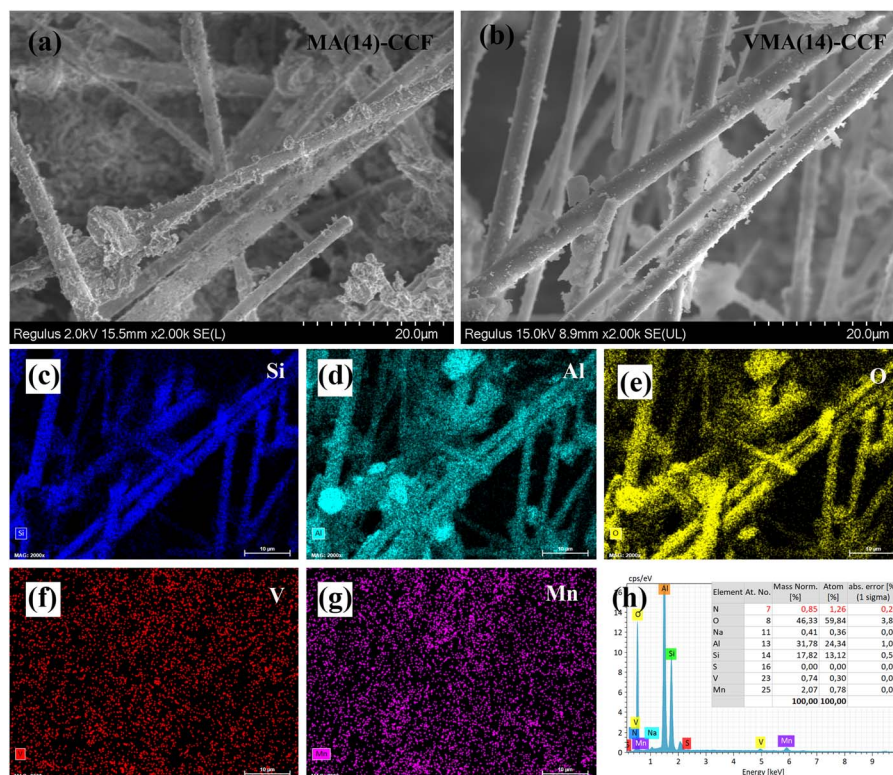
Fig. 3 SEM of MA(14)-CCF and VMA(14)-CCF.

denitration efficiency over a wide temperature range. The denitration performance of MA(14)-CCF, which was prepared with the same mass fraction of $Mn/\gamma\text{-}Al_2O_3$, was slightly higher than VMA(14)-CCF at 100–150 °C, and significantly lower than VMA(14)-CCF at 150–400 °C. This indicates that the addition of V can improve the denitration efficiency of the catalyst at medium to high temperatures.

3.2 Characterization

3.2.1 XRD. Fig. 2(b) shows the XRD spectra of MA(x)-CCF and VMA(y)-CCF. CF consists mainly of Al_2O_3 and SiO_2. MnO_x exists mainly in the form of $\beta\text{-}MnO_2$ (PDF#72-1983) and $\alpha\text{-}Mn_2O_3$ (PDF#71-0636). Vanadium oxide is mainly V_2O_4. And no peaks of V_2O_5 other than V_2O_4 were found. The state of the active components is an important factor affecting the catalyst's denitration activity.[17–19] The addition of V increases the peak intensity and crystallinity of MnO_x and $\gamma\text{-}Al_2O_3$ (PDF#81-2392), resulting in the agglomeration of MnO_x and the reduction of available active sites.[11,20,21] Meanwhile, the interaction between MnO_x and $\gamma\text{-}Al_2O_3$ is weakened, resulting in a decrease in NO conversion at low temperatures. With the increase in catalyst loading amount, the peak intensity of V_2O_5 and MnO_x in samples becomes stronger.

3.2.2 SEM. Fig. 3 shows the SEM results of MA(14)-CCF and VMA(14)-CCF. It can be observed that catalyst particles uniformly loaded on the interior and surface of CF, without obvious agglomerates. The catalyst particles of VMA(14)-CCF are smaller and more uniform than those of MA(14)-CCF. EDS characterization of VMA(14)-CCF at 20 μm depth shows that Si, Al, and O elements are mainly distributed on the ceramic fibers.

The mass percentage of Si is 13.12%, and the mass percentage of Al is 31.78%. The main components of the ceramic filter tube fibers are SiO_2 and Al_2O_3. The uniform distribution of V and Mn elements further confirms that the one-step coating method can successfully and effectively load the catalyst on the filter. Highly dispersed catalysts are favorable for exposing more active sites, increasing the contact surface area with the treated gas, and promoting efficient SCR reactions.[22]

3.2.3 XPS. To further investigate the atomic composition and elemental speciation on the surface of catalysts, XPS characterization was performed on $Mn/\gamma\text{-}Al_2O_3$ and $V\text{–}Mn/\gamma\text{-}Al_2O_3$.

Fig. 4(a) shows the XPS spectra of V2p, where the peak at 515.2–517.7 eV can be attributed to V^{4+}, while the peak at around 516.2–518.7 eV corresponds to V^{5+}.[23–25] The main forms of V_2O_5 species are V_2O_5 and V_2O_4, with a higher content of V^{5+} than V^{4+}. However, no diffraction peaks of V_2O_5 were detected in XRD, indicating that V_2O_5 is highly dispersed on the surface of the $\gamma\text{-}Al_2O_3$ support in an amorphous state. The $V_2O_9H_8$ structure formed by the combination of V_2O_5 with H_2O exhibits more Brønsted acid sites.[24]

The binding energy spectra of Mn 2p for the samples are shown in Fig. 4(b). The spectra include two characteristic peaks, Mn $2p_{1/2}$ and Mn $2p_{3/2}$. The Mn $2p_{3/2}$ peaks correspond to Mn^{3+} (642.03–643.38 eV) and Mn^{4+} (643.53–644.38 eV) species,[26,27] indicating that MnO_x in the catalyst mainly exists as a combination of Mn^{3+} and Mn^{4+}, which is consistent with the XRD results. According to Table 2, the percentage of Mn^{4+} in $V\text{–}Mn/\gamma\text{-}Al_2O_3$, indicates a strong interaction between V and Mn, and the doping of V promotes the conversion of Mn^{3+} to Mn^{4+}. Liu et al.[14] loaded Mn on V/Ti catalyst to modify its low-temperature
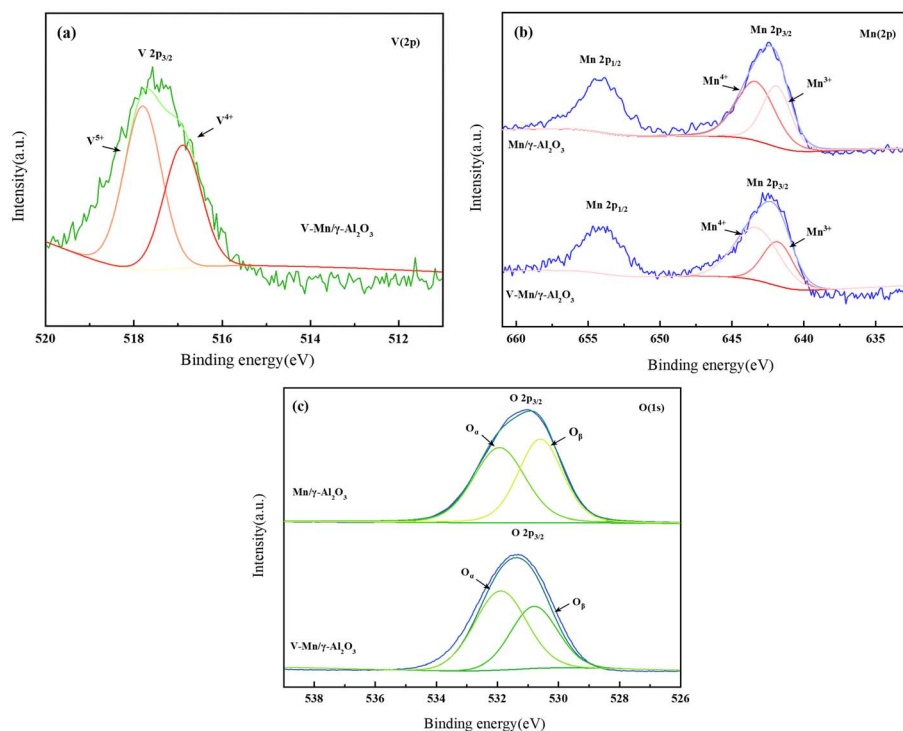

Fig. 4 XPS spectra of $Mn/\gamma\text{-}Al_2O_3$ and $V\text{–}Mn/\gamma\text{-}Al_2O_3$.

Table 2 The ratio of $V^{4+}/(V^{4+} + V^{5+})$, $Mn^{4+}/(Mn^{4+} + Mn^{3+})$ and $O_\alpha/(O_\alpha + O_\beta)$ of $Mn/\gamma\text{-}Al_2O_3$ and $V\text{-}Mn/\gamma\text{-}Al_2O_3$

Test samples	$V^{4+}/(V^{4+} + V^{5+})$	$Mn^{4+}/(Mn^{4+} + Mn^{3+})$	$O_\alpha/(O_\alpha + O_\beta)$
$Mn/\gamma\text{-}Al_2O_3$	—	57.1%	53.3%
$V\text{-}Mn/\gamma\text{-}Al_2O_3$	41.6%	70.5%	61.1%

Table 3 BET, pore volume, and average pore size of VMA(14)-CCF and MA(14)-CCF

Sample	Specific surface area/($m^2\ g^{-1}$)	Pore volume/($cm^3\ g^{-1}$)	Average pore size/(nm)
VMA(14)-CCF	47.45	0.17	8.20
MA(14)-CCF	48.22	0.18	8.54

SCR activity, and the results showed that the addition of MnO_x enhanced the REDOX ability of V. $Mn^{4+}\text{-}O^{2-}\text{-}V^{5+} \leftrightarrow Mn^{4+}\text{-}O^{2-}\text{-}V^{4+} \leftrightarrow Mn^{3+}\text{-}O^{2-}\text{-}V^{5+} \leftrightarrow Mn^{4+}\text{-}O^{2-}\text{-}V^{5+} + e$. This cycle can well control the electron movement between Mn and V, and ensure the REDOX capacity of the active species. The SCR activity at low temperature was improved and the original SCR activity at high temperature was maintained. Kapteijn et al.[28,29] reported that the NO conversion of pure manganese oxides follows the order: $MnO_2 > Mn_5O_8 > Mn_2O_3 > Mn_3O_4$. Since Mn^{4+} in manganese oxides has a higher oxidation state, it can promote the conversion of NO to NO_2, thereby facilitating the rapid SCR reaction.[30,31]

Fig. 4(c) shows the O 1s spectra of $Mn/\gamma\text{-}Al_2O_3$ and $V\text{-}Mn/\gamma\text{-}Al_2O_3$. Generally, there are two types of oxygen species on the catalyst surface, surface adsorbed oxygen and lattice oxygen (O^{2-}), denoted as O_α and O_β.[32–34] Surface adsorbed oxygen can further be classified into physically adsorbed oxygen and chemically adsorbed oxygen, which have higher mobility and reactivity compared to lattice oxygen, such as O_2, oxygen vacancies (O^{2-}, O_2^{2-}), or hydroxyl groups (OH^-).[35] The binding energy corresponding to O_α of $V\text{-}Mn/\gamma\text{-}Al_2O_3$ is 532 eV, shifted 0.1 eV to the left compared to O_α of $Mn/\gamma\text{-}Al_2O_3$. The binding energy corresponding to O_β is 530.9 eV, shifted 0.4 eV to the left compared to the lattice oxygen peak of $Mn/\gamma\text{-}Al_2O_3$. This indicates that V changes the electron binding energy of some oxygen atoms, causing the peaks of lattice oxygen and surface adsorbed oxygen to shift to higher binding energies.[36,37] Meanwhile, the addition of V increases the proportion of O_α in the catalyst, which has higher mobility and activity compared to O_β. In a word, the presence of V promotes electron transfer and redox capability of the catalyst.

3.2.4 BET. The N_2 adsorption–desorption experiments were conducted on VMA(14)-CCF and MA(14)-CCF (Fig. 5). The results are shown in Fig. 5. The specific surface area, total pore volume, and average pore size were calculated using the BET and BJH models (Table 3). According to the standard isotherms

for physical adsorption defined by the International Union of Pure and Applied Chemistry (IUPAC), the N_2 adsorption–desorption isotherms of the two samples all exhibit Ⅲ isotherms. The adsorption branch line on the curve does not overlap with the desorption branch line, which is caused by the presence of hysteresis loops and is usually associated with capillary condensation. The existence of hysteresis loop suggests that the catalysts are mainly composed of mesopores or micropores. The H4 hysteresis loops of VMA(14)-CCF and MA(14)-CCF indicate the presence of many micropores.

A larger specific surface area is favorable for gas adsorption, and a well-defined pore structure promotes the transfer of reactants between gas and catalyst, thereby enhancing the SCR reaction rate and significantly influencing the denitration activity of the catalysts.[38] The specific surface area, pore volume, and pore size of VMA(14)-CCF are slightly smaller than those of MA(14)-CCF. And there is no big difference, because the catalyst content of CCF is only 14%.

3.3 Catalytic activity test of the VMA(14)-CCF

3.3.1 Effect of FV on the SCR catalytic activity and pressure drop. The experiment changes the total gas to alter the face velocity (FV) of VMA(14)-CCF. When the gas flow is large, the FV is high, resulting in short residence time of gas in VMA(14)-CCF, and shorter contact time with the catalyst. When the gas flow is small, the FV is low, resulting in longer residence time of gas in VMA(14)-CCF, allowing for more complete contact and reaction with the catalyst, but this increases gas processing time. Therefore, determining the appropriate FV is of great significance for the industrial application of CCF. As shown in Fig. 6(a), when the FV is 0.6 m min^{-1}, the NO conversion of VMA(14)-CCF is greater than 80% at 150–400 °C; at 200–300 °C, the NO conversion can reach 100%. When the FV is 0.8 m min^{-1}, the NO conversion is greater than 80% at 200–350 °C; at 200–300 °C, the NO conversion can reach 100%. With the FV
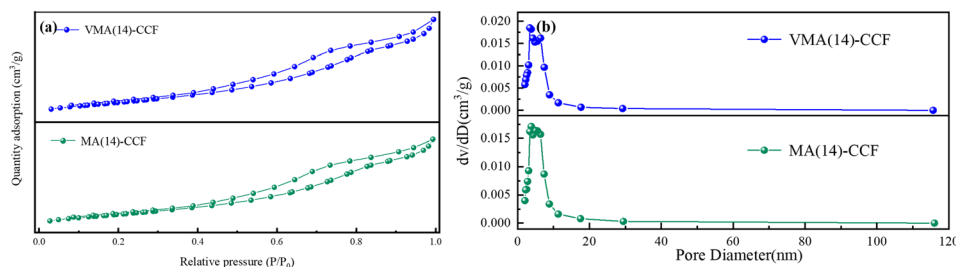
Fig. 5 N_2 absorption and desorption curves and pore size distribution of VMA(14)-CCF and MA(14)-CCF.
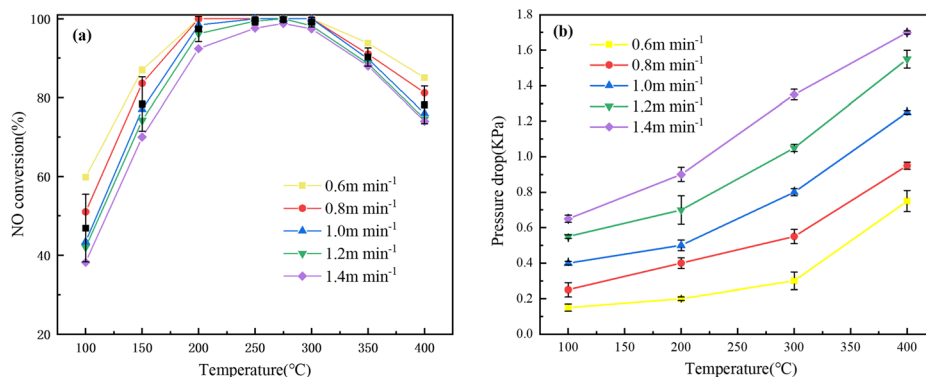
Fig. 6 (a) NO conversion and (b) Pressure drop of VMA(14)-CCF with different FV.

increased to 1.2 m min^{-1}, the NO conversion is greater than 80% at 200–350 °C. When the FV is 1.4 m min^{-1}, the NO conversion is greater than 80% at 200–350 °C. In industrial applications, when the FV is small, the applicable temperature range is 150–400 °C, while the FV is large, it can only be applied to flue gas treatment within the range of 200–350 °C.

The increase in temperature will cause the gas molecules to move faster, which will increase the pressure drop of the filter. Excessively high FV will also increase the pressure drop across the filter, not only causing resistance to dust removal, but also increasing the risk of unstable operation of the equipment. As shown in Fig. 6(b), the pressure drop of VMA(14)-CCF at various FV is relatively low. This may be due to the smaller particle size of V–Mn/γ-Al$_2$O$_3$ under the same loading amount, which is not easy to block the pores of the ceramic fibers, as confirmed in SEM. When the FV is 0.6 m min^{-1}, the pressure drop at 400 °C is only 0.75 kPa. The actual FV used in industrial factories is generally around 1 m min^{-1}, and the pressure drop of VMA(14)-CCF is 0.4 kPa at 100 °C, 0.5 kPa at 200 °C, 0.8 kPa at 300 °C, and 1.25 kPa at 400 °C. At 400 °C, the maximum pressure drop of VMA(14)-CCF is 1.7 kPa, greatly increasing the applicability of this filter.

3.3.2 Effect of SO$_2$ and H$_2$O on the SCR catalytic activity. In actual flue gas from factories, SO$_2$ and H$_2$O are widely present and have toxic effects on catalysts, further limiting the activity of catalysts.[39,40] Therefore, the tolerance of SO$_2$ and H$_2$O for

VMA(14)-CCF should be tested under conditions of 225 °C, 0.05% NO, 0.05% NH$_3$, and 3 vol% O$_2$ (Fig. 7(a)). Under the action of 100 ppm SO$_2$, VMA(14)-CCF maintained 100% denitrification efficiency within 300 min. After introducing 10% H$_2$O into the reaction gas, the NO conversion of VMA(14)-CCF was not affected within 5 h, indicating excellent sulfur and water resistance of VMA(14)-CCF. Under the same conditions, when 100 ppm SO$_2$ and 10% H$_2$O were added simultaneously, the NO conversion of VMA(14)-CCF was slightly affected, with the lowest decreasing to 99.4%, indicating a synergistic effect of H$_2$O and SO$_2$ in jointly inhibiting the catalytic activity.[39]

Since VMA(14)-CCF shows good sulfur resistance under 100 ppm SO$_2$ concentration, and some industries such as power generation, steelmaking, and building materials are prone to high-temperature oxygen-rich environments in their production processes, resulting in higher SO$_2$ content in flue gas. Therefore, the denitrification performance of VMA(14)-CCF was tested under 300 ppm SO$_2$. Within 1 h, VMA(14)-CCF still maintained 100% NO conversion, and then gradually decreased to 86.8% within 140 min. After cutting off the supply of SO$_2$, it recovered to 98.6% within 60 min, which was consistent with the performance before introduction. MA-CCF with the same catalyst loading amount of 14% was selected for the 300 ppm SO$_2$ test, and the NO conversion decreased rapidly within the first 100 min, reaching a minimum of 70.6%. Afterward, the decrease was slower, with a minimum of 63.2%. It was 23.6
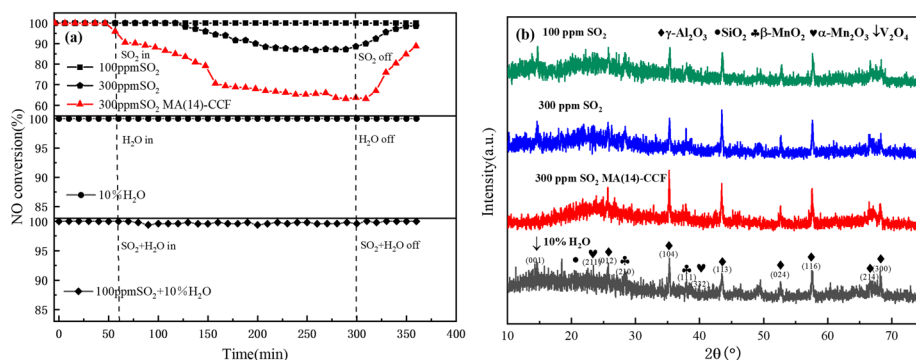

Fig. 7 (a) NO conversion and (b) XRD spectrum of VMA(14)-CCF and MA(14)-CCF in the presence of SO$_2$ and H$_2$O at 225 °C.
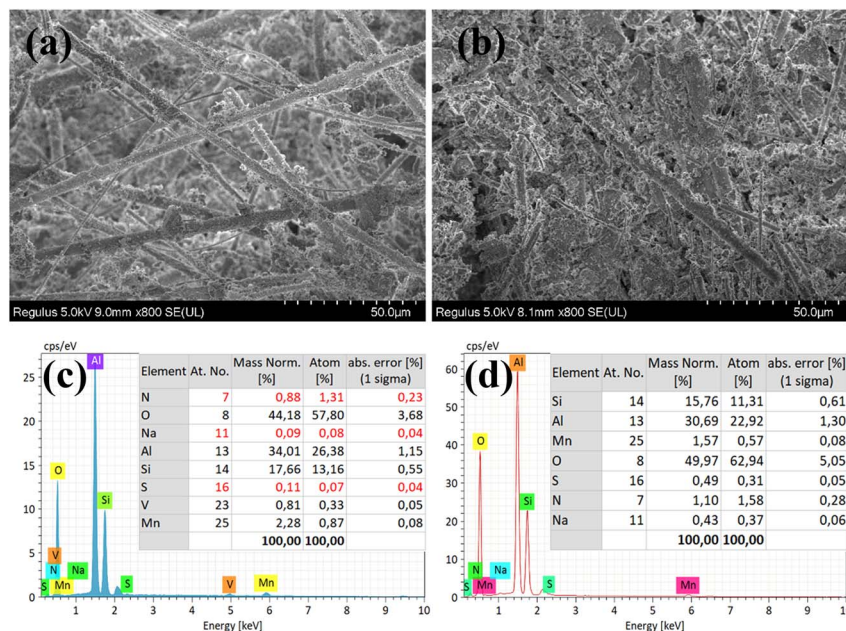
Fig. 8 (a) SEM and EDS of VMA(14)-CCF and MA(14)-CCF after 300 ppm SO_2 at 225 °C.

percentage points lower than that of VMA(14)-CCF under the same environment. This indicates that MnO_x is more affected by SO_2, and manganese-based catalysts are not suitable for application in high-sulfur environments. V_2O_5 has good sulfur resistance, and the introduction of vanadium can broaden the applicable range of MnO_x.

The VMA(14)-CCF after environmental testing with 100 ppm SO_2 and 10% H_2O was characterized by XRD, and the results showed no significant changes compared to the VMA(14)-CCF before the experiment (Fig. 7(b)). Higher Mn^{4+} concentration plays a critical role in the SCR activity, as evidenced by XPS characterization results indicating that the introduction of V promotes the conversion of Mn^{3+} to Mn^{4+}. Higher Mn^{4+} concentration enhances the catalyst's catalytic reduction ability and improves its resistance to sulfur and water.[41] The impact of SO_2 on the catalyst can be summarized in three aspects: first, SO_2 reacts with NH_3 to form $(NH_4)_2SO_4$ or NH_4HSO_4, which blocks the active sites of the catalyst and hinders the reaction between NO_x and the active sites;[31,42] second, SO_2 competes with NO for adsorption, leading to a decrease in the conversion rate of nitrogen oxides by the catalyst;[43,44] third, SO_2 reacts with active components to form inert metal sulfates, which reduces the quantity of catalyst available for gas reactions and leads to a decrease in denitration performance.[39,45] XRD and SEM characterization of VMA(14)-CCF and MA(14)-CCF after anti-sulfur experiments with 300 ppm revealed that the MnO_x peak disappeared in MA(14)-CCF, while the MnO_x in VMA(14)-CCF showed no significant change compared to before the experiment (Fig. 8). SEM combined with EDS results showed block-like substances larger than the catalyst particle size in MA(14)-CCF, with S content of 0.32%. In contrast, particles on the ceramic fibers of VMA(14)-CCF were still uniformly distributed, with only a small amount of small block-like substances and S content of only 0.07%. Combined with XPS results, the addition of V_2O_5 provides more surface adsorbed oxygen for the catalyst, allowing NH_3 to react with the abundant surface adsorbed
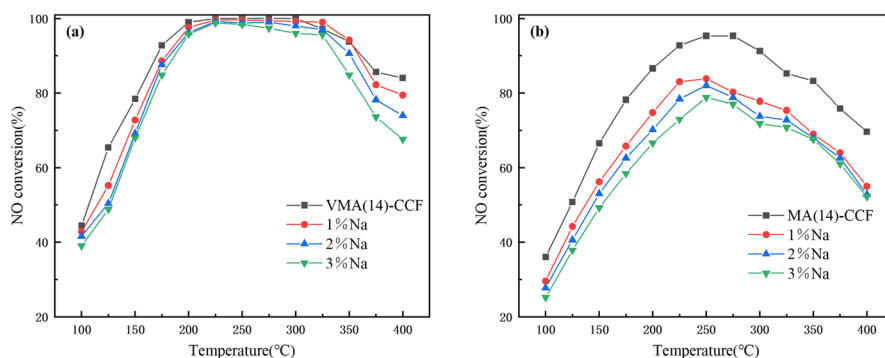

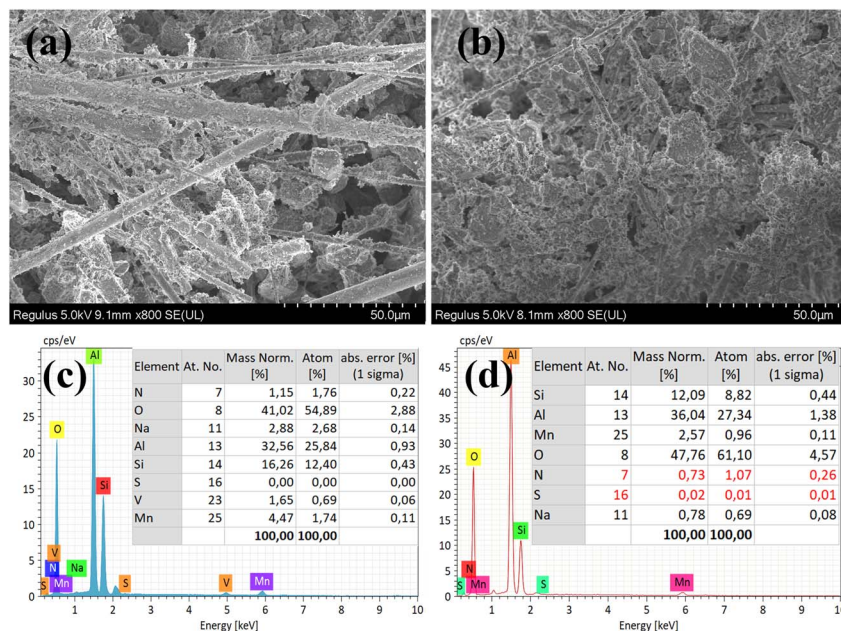**Fig. 9** NO conversion of (a) VMA(14)-CCF and (b) MA(14)-CCF in the presence of Na.

Fig. 10 (a) SEM and EDS of VMA(14)-CCF and MA(14)-CCF after 3% Na.

Table 4 BET, pore volume, and average pore size of VMA(14)-CCF and MA(14)-CCF after 3% Na

Sample	Specific surface area/($m^2\ g^{-1}$)	Pore volume/($cm^3\ g^{-1}$)	Average pore size/(nm)
3% Na-VMA(14)-CCF	46.41	0.11	9.54
3% Na-MA(14)-CCF	40.56	0.10	8.34

oxygen even in the presence of SO_2, resulting in less formation of $(NH_4)_2SO_4$ or NH_4HSO_4. On the other hand, in the presence of SO_2, active V_2O_5 preferentially react with SO_2, protecting the active centers of MnO_x and reducing the degree of catalyst poisoning by SO_2.

3.3.3 Effect of Na on the SCR catalytic activity. Alkali in the flue gas is one of the important factors causing catalyst deactivation.[46,47] The main sources of alkali in production are fuel combustion, lubricant additives, urea, *etc.* As shown in Fig. 9(a), the addition of Na had a relatively small effect on VMA(14)-CCF. However, the addition of Na significantly reduced the denitration efficiency of MA(14)-CCF, as shown in Fig. 9(b). The largest decrease in denitration efficiency occurred at 275 °C, with a 15.1% decrease in denitration efficiency with 1% Na addition. With the increase of Na content, the NO conversion at various temperatures decreased slightly.

EDS and BET characterization were performed on MA(14)-CCF and VMA(14)-CCF after treatment with 3% Na, and the results are shown in Fig. 10 and Table 4. The content of Na in both samples increased, and block-like substances were observed to adhere to the surface in the electron microscope images. Moreover, the specific surface area and pore volume of MA(14)-CCF and VMA(14)-CCF decreased. This indicates the sodium compound is enriched and deposited on the surface of the catalyst's active sites, blocking the pores and reducing the

activity centers for gas treatment. In addition, the addition of alkali metals generates basic centers after the reaction, which enhances the alkalinity of the catalyst surface and reduces its adsorption capacity for NH_3.[48] At the same time, the addition of alkali metals also weakens the catalytic reducibility of the catalyst, and multiple factors lead to a decrease in denitration efficiency of the catalyst, consistent with the experimental results.[49] Although the specific surface area of the two samples is similar, the alkali resistance of VMA(14)-CCF is significantly better than that of MA(14)-CCF, due to the close relationship between the redox performance and alkali resistance of the catalyst. The presence of V_2O_5 results in a more abundant surface adsorbed oxygen and Mn^{4+}, which enhances the surface acidity and redox properties of the catalyst, making VMA(14)-CCF exhibit excellent alkali resistance and maintain high NO conversions in experiments with different alkali metal mass fractions.

4 Conclusions

A novel ceramic filter for selective catalytic reduction of NO_x catalyst was developed. The ceramic fibers retain their original shape. The catalyst particles are uniformly distributed on CF, and the denitration effect is not affected by the loading process. The feasibility of Mn-based CCF modified by V is proved. When

the FV is 1 m min^{-1}, the NO conversion rate of VMA(14)-CCF reaches more than 80% at 175–400 °C, and 100% at 225–300 °C. It shows excellent denitration efficiency over a wide temperature range. High NO conversion and low pressure drop can be maintained at various filtration speeds. It has excellent resistance to water, sulfur and alkali metal poisoning. The possibility of practical application and popularization of VMA(14)-CCF is greatly increased. Its strong anti-poisoning ability is due to the introduction of V not only protects the active center of MnO$_x$, but also promotes the transformation of Mn^{3+} to Mn^{4+}. This provides abundant surface adsorbed oxygen for the catalyst, and enhances the adsorption of NH$_3$ and NO by the catalyst, thus improving the surface acidity and oxidation reducibility of the catalyst.

Author contributions

Lei Sun: writing – investigation, original draft, methodology, date curation, formal analysis, funding acquisition, visualization. Zhenzhen Wang: methodology, writing – review & editing, software. Mengxi Zang: formal analysis.

Conflicts of interest

The authors declared that they have no conflicts of interest to this work.

Acknowledgements

References

1 T. Wang, C. Zhu, H. Liu, Y. Xu, X. Zou, B. Xu and T. Chen, *Environ. Technol.*, 2018, **39**, 317–326.

2 Z. Wang, S. Peng, C. Zhu, B. Wang, B. Du, T. Cheng, Z. Jiang and L. Sun, *RSC Adv.*, 2023, **13**, 344–354.

3 W. Zhang, K. Xie, Y. Tang, S. Cheng, M. Qing, Y. Xuan, C. Qin, M. Dong, Y. Zhou and J. Li, *RSC Adv.*, 2022, **12**, 22881–22892.

4 J. Kim, D. W. Kwon, S. Lee and H. P. Ha, *Appl. Catal., B*, 2018, **236**, 314–325.

5 X. Yang, L. Kang, C.-J. Wang, F. Liu and Y. Chen, *Chem. Commun.*, 2021, **57**, 7176–7179.

6 S. Youn, S. Jeong and D. H. Kim, *Catal. Today*, 2014, **232**, 185–191.

7 L. Zhao, K. Li, R. Wu, H. Zhang and J. Jin, *Mater. Res. Express*, 2020, **7**, 125502.

8 Y.-s. Zhang, C. Li, C. Wang, J. Yu, G. Xu, Z.-g. Zhang and Y. Yang, *Ind. Eng. Chem. Res.*, 2019, **58**, 828–835.

9 H. Lin, Z. Chen, C. Li, X. Yao, Z. Yao, G. Xu, S. Gao, X. Huang and J. Yu, *Catalysts*, 2020, **10**, 2073–4344.

10 M. Zhu, J.-K. Lai, U. Tumuluri, M. E. Ford, Z. Wu and I. E. Wachs, *ACS Catal.*, 2017, **7**, 8358–8361.

11 Z. Fan, J.-W. Shi, C. Gao, G. Gao, B. Wang, Y. Wang, C. He and C. Niu, *Chem. Eng. J.*, 2018, **348**, 820–830.

12 L. Xu, S. Niu, C. Lu, Q. Zhang and J. Li, *Fuel*, 2018, **219**, 248–258.

13 S. Zhang, Y. Zhao, J. Yang, J. Zhang and C. Zheng, *Chem. Eng. J.*, 2018, **348**, 618–629.

14 Z. Liu, Y. Li, T. Zhu, H. Su and J. Zhu, *Ind. Eng. Chem. Res.*, 2014, **53**, 12964–12970.

15 T. H. Vuong, S. Bartling, U. Bentrup, H. Lund, J. Rabeah, H. Atia, U. Armbruster and A. Brückner, *Catal. Sci. Technol.*, 2018, **8**, 6360–6374.

16 Y. Niu, T. Shang, S. Hui, X. Zhang, Y. Lei, Y. Lv and S. Wang, *Fuel*, 2016, **185**, 316–322.

17 W. Li, X. Du, Z. Li, Y. Tao, J. Xue, Y. Chen, Z. Yang, J. Ran, V. Rac and V. Rakić, *Process Saf. Environ. Prot.*, 2022, **159**, 213–220.

18 G. Zhai, Z. Han, X. Wu, H. Du, Y. Gao, S. Yang, L. Song, J. Dong and X. Pan, *J. Taiwan Inst. Chem. Eng.*, 2021, **125**, 132–140.

19 R. Li, Y. Liang, Z. Zhang, Q. Huang, X. Jiang, R. Yang, L. Yu and J. Jiang, *Catal. Today*, 2022, **405–406**, 125–134.

20 T. Qiao, Z. Liu, C. Liu, W. Meng, H. Sun and Y. Lu, *Appl. Catal., A*, 2021, **617**, 118128.

21 X. Shi, J. Guo, T. Shen, A. Fan, S. Yuan and J. Li, *Chem. Eng. J.*, 2021, **421**, 129995.

22 R. Xiao, T. Gao, X. Cui, Y. Ji, Y. Zhang, X. Chuai, Z. Xiong, Y. Liao, H. Gu, J. Yang, J. Zhang and Y. Zhao, *Fuel*, 2022, **310**, 122219.

23 N. Zhu, W. Shan, Z. Lian, Y. Zhang, K. Liu and H. He, *J. Hazard. Mater.*, 2020, **382**, 120970.

24 S. Soyer, A. Uzun, S. Senkan and I. Onal, *Catal. Today*, 2006, **118**, 268–278.

25 A. Abubakar, C. Li, L. Huangfu, S. Gao and J. Yu, *Korean J. Chem. Eng.*, 2020, **37**, 633–640.

26 Z. Li, Y. Gao and Q. Wang, *J. Cleaner Prod.*, 2022, **348**, 131152.

27 K. Zheng, Z. Zhou, Y. Wang, Z. Xin, Z. Zhao, J. Zhang, T. Bo, T. Lin, B. Zhang and L. Shao, *Catal. Sci. Technol.*, 2020, **10**, 3450–3457.

28 F. Kapteijn, L. Singoredjo, A. Andreini and J. A. Moulijn, *Appl. Catal., B*, 1994, **3**, 173–189.

29 S. Boxiong, M. Hongqing, H. Chuan and Z. Xiaopeng, *Fuel Process. Technol.*, 2014, **119**, 121–129.

30 B. Tian, S. Ma, Y. Zhan, X. Jiang and T. Gao, *Appl. Surf. Sci.*, 2021, **541**, 148460.

31 J. Chen, P. Fu, D. Lv, Y. Chen, M. Fan, J. Wu, A. Meshram, B. Mu, X. Li and Q. Xia, *Chem. Eng. J.*, 2021, **407**, 127071.

32 Y. Zhang, C. Hao, J. Zhang, J. Wu, Y. Yue, Y. Xu and G. Qian, *Colloids Surf., A*, 2022, **635**, 128080.

33 J.-K. Lai, N. R. Jaegers, B. M. Lis, M. Guo, M. E. Ford, E. Walter, Y. Wang, J. Z. Hu and I. E. Wachs, *ACS Catal.*, 2021, **11**, 12096–12111.

34 S. Ji, P. Li, X. Zhao, S. Wei, X. Cheng, L. Wu, Y. Ye, K. Ma, Y. Cai and C. Liang, *Sens. Actuators, B*, 2023, **383**, 133595.

35 T. Cheng, B. Du, H. Zhou, Z. Jiang, Q. Xie and C. Zhu, *Environ. Sci. Pollut. Res.*, 2023, **30**, 36294–36310.

36 S. Dong, H. Wang, L. Gong, R. Hu and Z. Qu, *Surf. Interfaces*, 2022, **35**, 102411.

37 Z. Lyu, S. Niu, K. Han, C. Lu and Y. Li, *Appl. Catal., A*, 2021, **610**, 117968.

38 X. Zhou, X. Huang, A. Xie, S. Luo, C. Yao, X. Li and S. Zuo, *Chem. Eng. J.*, 2017, **326**, 1074–1085.

39 S. W. Jeon, I. Song, H. Lee, J. Kim, Y. Byun, D. J. Koh and D. H. Kim, *Chem. Eng. J.*, 2022, **433**, 133836.

40 L. Xie, C. Liu, Y. Deng, F. Liu and W. Ruan, *Ind. Eng. Chem. Res.*, 2022, **61**, 8698–8707.

41 B. Du, Y. Hu, T. Cheng, Z. Jiang, Z. Wang and C. Zhu, *RSC Adv.*, 2023, **13**, 6378–6388.

42 B. Wang, B. Yao, F. Qi, S. Wang and B. Shen, *J. Fuel Chem. Technol.*, 2022, **50**, 503–512.

43 F. Wang, B. Shen, S. Zhu and Z. Wang, *Fuel*, 2019, **249**, 54–60.

44 Y. Shu, T. Aikebaier, X. Quan, S. Chen and H. Yu, *Appl. Catal., B*, 2014, **150–151**, 630–635.

45 C. Tang, H. Wang, S. Dong, J. Zhuang and Z. Qu, *Catal. Today*, 2018, **307**, 2–11.

46 P. Raghunath and M. C. Lin, *J. Phys. Chem. C*, 2008, **112**, 8276–8287.

47 H. Si-Ahmed, M. Calatayud, C. Minot, E. L. Diz, A. E. Lewandowska and M. A. Bañares, *Catal. Today*, 2007, **126**, 96–102.

48 J. Due-Hansen, S. Boghosian, A. Kustov, P. Fristrup, G. Tsilomelekis, K. Ståhl, C. H. Christensen and R. Fehrmann, *J. Catal.*, 2007, **251**, 459–473.

49 K. Guo, J. Ji, W. Song, J. Sun, C. Tang and L. Dong, *Appl. Catal., B*, 2021, **297**, 120388.